Soil Dynamics and Earthquake Engineering 147 (2021) 106773

Contents lists available at ScienceDirect

Soil Dynamics and Earthquake Engineering

journal homepage: www.elsevier.com/locate/soildyn

A hybrid boundary method for seismic wave propagation problems in slopes

Hao Wang [a,b], Chao Luo [a,b,*], Jun-Zhou Wan [b], Meng-Fan Zhu [b], Meng-Lin Lou [c], Huai-Ping Feng [a,b]

[a] State Key Laboratory of Mechanical Behavior and System Safety of Traffic Engineering Structures, Shijiazhuang Tiedao University, Shijiazhuang 050043, China
[b] School of Civil Engineering, Shijiazhuang Tiedao University, Shijiazhuang, Hebei Province, 050043, China
[c] State Key Laboratory of Disaster Reduction in Civil Engineering, Tongji University, Shanghai, 200092, China

ARTICLE INFO

Keywords:
Slope
Wave propagation
Hybrid boundary method
Ground motion
Artificial boundary

ABSTRACT

The seismic behavior of a slope site has a critical impact on its stability and the seismic response of structures located on or near the slope. In this paper, a hybrid boundary method(HBM) is proposed for the site response analysis of slopes. Viscous and viscous-spring boundaries are applied in the HBM and equivalent loads are calculated separately on the bottom and the lateral boundary. A horizontally extended model is used to verify the HBM. The results show that the maximum error of the HBM is only 2.010%. On the ground surface of the slope site, amplification occurs at the crest side and de-amplification occurs at the toe side under various cases. The ratio of the maximum and minimum PGA on the ground surface could exceed 2. Therefore, great attention should be paid to the spatial variability of ground motion on slope sites. The HBM is also compared with four conventional approaches. The maximum errors of all the conventional approaches exceed 70%. These examples demonstrate that the HBM has much higher accuracy in practice than conventional approaches.

1. Introduction

In the analysis of site response and earthquake–soil–structure interaction(ESSI) in localized regions, the soil layer are usually considered as a semi-infinite medium. The analytical solution exists for certain types of semi-infinite problems and has gained considerable attention over the past few decades. The earliest research dates back to 1878 when [1] proposed the analytical solution of the semi-infinite elastic body under the vertical static load. Since then, a great number of semi-infinite spatial static and dynamic analytical solutions were provided, such as the famous Lamb problem [2] , Mindlin solution [3] and Green's Function [4–7]. These analytical solutions provide options in solving the semi-infinite problems, but they can only be used in specific ideal conditions.

When problems get more complicated and the analytical solutions can hardly be obtained, researchers have to turn to numerical methods. One of the most widely used numerical methods in civil engineering is the finite element method (FEM). Given the FEM cannot simulate infinite or semi-infinite domains directly, a number of methods have been proposed to extend the application of FEM to semi-infinite space simulations. Alterman and Karal [8] first propose an simple and straightforward solution, that is building the FEM model as large as possible to simulate a semi-infinite space. This method is readily understood but very time-consuming and resource-consuming, especially for three-dimensional(3D) problems. The viscous boundary proposed by Lysmer and Kuhlemeyer [9] is another solution. By introducing dashpots at the boundary of a FEM model, the radiation energy from the excited zone to the far-field can be accounted for properly. The viscous boundary can absorb outwardly propagating waves on the boundary, but it does not provide elastic restoring force, which creates additional permanent displacements in practice. Researchers such as White et al. [10], Akiyoshi [11], Deeks and Randolph [12], Liu and Li [13] and Du and Zhao [14] improved the viscous boundary through different approaches. The improvement proposed by Liu and Li [13] has been widely used due to its stability and ease of implementation.

The methods mentioned above all focus on canceling the radiation energy from the excited zone to the far-field. In the analysis of site response and ESSI, the localized regions are usually relatively small compared to the distance between the fault and the local site. It is not economical and practical to build such a large model that includes both the fault and the local site. In practice, one solution is to build a local site model and use seismic input methods that take account of semi-infinite space characteristics. Joyner and Chen [15] proposed a method for one-dimensional(1D) wave propagation analysis. A horizontal equivalent force time history with dashpots at the base of the soil column was incorporated as the equivalent seismic excitation, which

---

[*] Corresponding author at: State Key Laboratory of Mechanical Behavior and System Safety of Traffic Engineering Structures, Shijiazhuang Tiedao University, Shijiazhuang 050043, China.

E-mail addresses: wanghao@stdu.edu.cn (H. Wang), luochao@stdu.edu.cn (C. Luo), hefeiwjz@163.com (J.-Z. Wan), 2544656543@qq.com (M.-F. Zhu), lml@tongji.edu.cn (M.-L. Lou), fenghuaiping@stdu.edu.cn (H.-P. Feng).

https://doi.org/10.1016/j.soildyn.2021.106773
Received 8 January 2021; Received in revised form 18 March 2021; Accepted 9 April 2021

was proportional to the density of bedrock, the shear wave velocity, and the velocity time history of outcrop motion. Based on Joyner's research, Yasui et al. [16] introduced angle dependent viscous dashpots for inclined seismic wave excitation. Based on the assumption that the displacement wave field and the stress wave field should be equal to those of free fields, Liu and Lu [17] proposed Liu's direct method(LDM) which extends the range of realizing the equivalent excitation from 1D wave propagation to inclined wave and multiple support excitation. Luo [18] proposed the Simplified Liu's Direct Method(SLDM), which only needs to use the free field motion on the boundary to calculate the equivalent loads and can simulate several kinds of realistic wave fields, including body waves and surface waves. Bielak and Yoshimura [19,20] proposed the Domain Reduction Method(DRM), calculating the effective loads by the free field motion on the boundary of the local site. The DRM is applicable to any kind of realistic wave and various kinds of absorbing boundaries. Due to its convenience and advancement in computational accuracy and efficiency, the DRM has been widely used in past decades [21–27]. It is worth noting that unlike the free field motion in some SSI papers, the free field motion in those methods mentioned above and this paper refers the wave solution in a domain with no topography and heterogeneity.

New challenges arise when the local sites are slopes. For 2D or 3D analysis of site response and ESSI, the free field motions at local boundaries are required to calculate the equivalent seismic loads. Whereas, there is no rational free field motion solution available for the slope sites when using the methods mentioned above. Thus, researchers have to make a compromise either by making use of approximate free-field motions or employing the rigid bedrock assumption. By adding additional layers to the original site and attach viscous dashpots, Ashford et al. [28],Ashford and Sitar [29] realized the simulation of the semi-infinite base of a steep slope in the frequency domain. Nevertheless, it was mentioned by the author that there was some scattered energy bounced back to the system. Bouckovalas and Papadimitriou [30] applied transmitting boundary at the base of the mesh and applied boundaries simulating the free field at its right and left side. However, the verification model was a semi-circular shaped canyon rather than a slope topography, and the width the slope was modeled 20 times its height to eliminate the lateral effects. Adopting the rigid bedrock assumption, Tripe et al. [31] discussed the interaction between topographic amplification effects and soil layer amplification effects of a slope in a homogeneous soil layer overlying bedrock by using the DRM. The results show that the influence of soil layer effect on ground motion is greater than that of topographic. Rizzitano et al. [32] built models based on the assumptions of rigid bedrock and elastic half-space to investigate the amplification of the ground motion induced by soil topography, but no artificial boundary conditions were applied on the lateral boundary. Researchers also employed shaking table tests or centrifuge tests to investigate the site response of slopes. The slope models were usually constructed and tested in a rigid box container and the rigid bedrock assumption instead of semi-infinite space assumption was used in these tests [33–36].

Based on the above studies, it can be seen that the existing methods cannot fully meet the requirements of the semi-infinite excitation simulation of slope sites. In this paper, a hybrid boundary method(HBM) is proposed to reveal the slope characteristics in site response analysis. The HBM uses different strategies to deal with bottom and horizontal boundaries. On the bottom boundary, viscous and viscous-spring boundaries are deployed. The calculation method of equivalent load on the bottom boundary is improved based on Joyner method, making it applicable for 2D/3D analysis. A SLDM is proposed for the lateral boundary, which only requires the free field displacements to compute the equivalent loads. Whereafter, a numerical example of the slope site is given to verify the effectiveness and accuracy of the proposed method. The seismic responses of the slope site under different excitation waves and excitation directions are investigated. The influence of slope inclination and damping on the validity of the HBM are also discussed. Afterward, the seismic responses of the slope are computed by other four approaches: (i) the SLDM with free field motion on crest side; (ii) the SLDM with free field motion on toe side; (iii) the SLDM with combined free field motions; (iv) fixed based method. The results of the proposed method and the other four approaches are compared and their computational accuracy is discussed. Finally, the reasonable evaluation indicator of time history results and the PGA (Peak Ground Motion) distribution along the slope surface are studied.

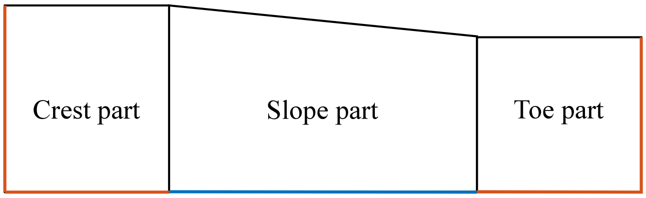

Fig. 1. Schematic of 2D slope site.

2. Methodology

For vertically propagating P/SV waves, the slope site has different free field motions but the same outcrop motion on the bottom boundary. Meanwhile, the analytical solution for 1D P/SV wave propagation can be used to approximated the free field motion solution on the lateral boundary. Therefore, the methods using the outcrop motion as a known condition is appropriate for the bottom boundary, and the methods using the free field motion as a known condition is appropriate for the lateral boundary. To satisfy the requirements of the semi-infinite excitation for slope sites, the bottom and lateral boundaries need to be dealt with differently.

2.1. Bottom boundary

As mentioned above, there is no analytical free-field motion solution of slope sites available for those widely used seismic input methods such as LDM and DRM. Also, the free field motion at bottom boundary of a slope site various at different parts in Fig. 1. However, the outcrop motion of the three parts are the same. Installing viscous damper at the bottom of the model based on the Joyner's method [15], the effective excitation forces can be expressed as

$$f(t) = 2A\rho v_s \dot{y}(t) \tag{1}$$

where ρ and v_s are the density and the shear wave velocity of the underlying soil respectively. $\dot{y}(t)$ is the velocity time history of the outcrop motion. A is the area that each node represents. Since the topography produces vertical motions, additional viscous-spring boundaries in the vertical direction will also be installed at the bottom of the model in 2D/3D analysis to avoid unnecessary reflections at the boundary. Taking a 2D slope model shown in Fig. 1 as an example, When the slope model is excited in the horizontal direction, the viscous boundary is installed in the horizontal direction and the viscous-spring boundary is installed in the vertical direction at the bottom boundary. When the model is excited in vertical direction, the viscous boundary is installed in the vertical direction and viscous-spring boundary is installed in the horizontal direction. Also note that the shear wave velocity v_s in Eq. (1) should be replaced by the compression wave velocity v_p when the input motion only has a vertical component. When the slope model is excited in multiple directions, the viscous-spring boundaries should be installed in all the directions. Then the effective load calculated by Eq. (1) can be adjusted to the following forms:

$$\mathbf{f}(t) = \begin{Bmatrix} f_x(t) \\ f_y(t) \end{Bmatrix} = A \cdot \begin{Bmatrix} 2\rho v_s \dot{y}_s(t) + K_{bx} u_x(t) \\ 2\rho v_p \dot{y}_p(t) + K_{by} u_y(t) \end{Bmatrix} \tag{2}$$

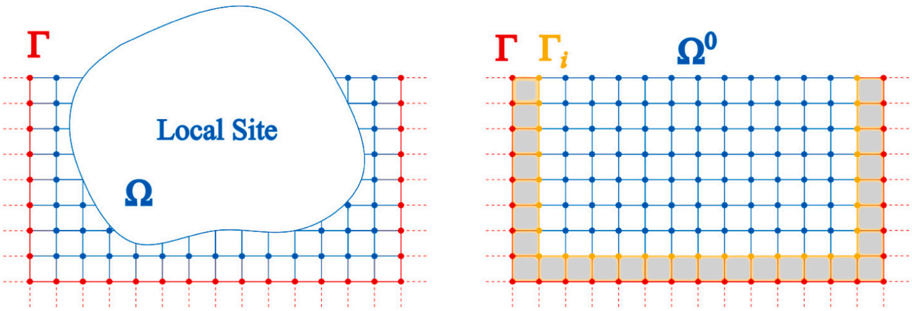

(a) local site model (b) free field model

Fig. 2. Scheme of SLDM: local site model and free field model.

where v_p denotes the compression wave velocity of the underlying soil; $\dot{y}_s$ and $\dot{y}_p$ are the velocity time history of P and SV wave outcrop motion; K_{bx} and K_{bx} are the stiffness coefficient of the bottom boundary in horizontal and vertical direction, respectively; $u_x(t)$ and $u_y(t)$ are the free field displacement on the boundary in x and y direction, respectively. Eq. (2) can also be extended to 3D domain, by using the shear wave parameters in the east–west and north–south directions and compression wave parameters in the up–down directions. As mentioned before, there is no analytical solution for $u_x(t)$ and $u_y(t)$, one can only use 1D wave propagation solutions for approximation. These free field displacement will introduce errors, which will be discussed in the following sections.

2.2. Lateral boundary

It is easy to obtain the free field motions at the lateral boundary through 1D wave propagation analysis. Therefore, any seismic input method that only requires free-field motion as a known condition is applicable here, such as the LDM [17] and the DRM [19,20]. In this paper, the SLDM [18] is proposed which reduces the required known conditions of the LDM.

2.2.1. Simplified Liu's direct method

Based on LDM [13], the SLDM is a finite element method that simulates wave propagation in the semi-infinite medium. This method needs to apply effective nodal forces on a finite element model with viscous or viscous-spring boundary conditions to realize the semi-infinite excitation. A 2D example of a semi-infinite region is shown in Fig. 2(a). The boundary Γ and domain Ω denote the truncated boundary of the local site model and local computing domain respectively. In SLDM, the local boundaries connect with viscous-spring boundary, which is, all the red nodes in Fig. 2(a) are assembled with viscous-spring boundary. Therefore, the equation of a SLDM local site model can be expressed as in partitioned form as [37]:

$$\begin{bmatrix} M_{ii}^{\Omega} & M_{ib}^{\Omega} \\ M_{bi}^{\Omega} & M_{bb}^{\Omega} \end{bmatrix}\begin{Bmatrix} \ddot{u}_i \\ \ddot{u}_b \end{Bmatrix} + \begin{bmatrix} C_{ii}^{\Omega} & C_{ib}^{\Omega} \\ C_{bi}^{\Omega} & C_{bb}^{\Omega}+C_b \end{bmatrix}\begin{Bmatrix} \dot{u}_i \\ \dot{u}_b \end{Bmatrix} + \begin{bmatrix} K_{ii}^{\Omega} & K_{ib}^{\Omega} \\ K_{bi}^{\Omega} & K_{bb}^{\Omega}+K_b \end{bmatrix}\begin{Bmatrix} u_i \\ u_b \end{Bmatrix} = \begin{Bmatrix} 0 \\ P_{eff} \end{Bmatrix} \tag{3}$$

where K, M and C denote the stiffness, mass and damping matrices; i and b refer to nodes in the interior domain or on the boundary Γ; u denotes the displacement of the system; C_b and K_b denotes the damping and stiffness terms of the viscous-spring boundary. As shown in Fig. 3, the excitation P_{eff} can be divided into two components: (1) Nodal forces P_{fre} that makes the stress and displacement at the model boundary the same as the original free field model before the artificial boundary conditions are applied; (2) Nodal force P_{vs} that makes the displacement of the viscous spring boundary consistent with the free-field response. The effective nodal force P_{eff} on the boundary Γ can be expressed as

$$P_{eff} = P_{fre} + P_{vs} \tag{4}$$

Based on the definition of P_{vs}, the calculation of P_{vs} can be expressed as follows [17]

$$P_{vs} = C_b\dot{u}_b^0 + K_b u_b^0 \tag{5}$$

where C_b and K_b are damping and stiffness matrices of the viscous spring boundary.

According to the definition of P_{fre}, a free field model shown in Fig. 2(b) which removes all the local features is introduced, Then the equation of the free field model can be written in blocks as:

$$\begin{bmatrix} M_{ii}^{\Omega^0} & M_{ib}^{\Omega^0} \\ M_{bi}^{\Omega^0} & M_{bb}^{\Omega^0} \end{bmatrix}\begin{Bmatrix} \ddot{u}_i^0 \\ \ddot{u}_b^0 \end{Bmatrix} + \begin{bmatrix} C_{ii}^{\Omega^0} & C_{ib}^{\Omega^0} \\ C_{bi}^{\Omega^0} & C_{bb}^{\Omega^0} \end{bmatrix}\begin{Bmatrix} \dot{u}_i^0 \\ \dot{u}_b^0 \end{Bmatrix} + \begin{bmatrix} K_{ii}^{\Omega^0} & K_{ib}^{\Omega^0} \\ K_{bi}^{\Omega^0} & K_{bb}^{\Omega^0} \end{bmatrix}\begin{Bmatrix} u_i^0 \\ u_b^0 \end{Bmatrix} = \begin{Bmatrix} 0 \\ P_{fre} \end{Bmatrix} \tag{6}$$

where the Ω^0 denotes the free field domain of Ω. Then equation can be written separately as follows:

$$M_{ii}^{\Omega^0}\ddot{u}_i^0 + C_{ii}^{\Omega^0}\dot{u}_i^0 + K_{ii}^{\Omega^0}u_i^0 = -M_{ib}^{\Omega^0}\ddot{u}_b^0 - C_{ib}^{\Omega^0}\dot{u}_b^0 - K_{ib}^{\Omega^0}u_b^0 \tag{7}$$

$$P_{fre} = M_{bi}^{\Omega^0}\ddot{u}_i^0 + M_{bb}^{\Omega^0}\ddot{u}_b^0 + C_{bi}^{\Omega^0}\dot{u}_i^0 + C_{bb}^{\Omega^0}\dot{u}_b^0 + K_{bi}^{\Omega^0}u_i^0 + K_{bb}^{\Omega^0}u_b^0 \tag{8}$$

It can be deduced from Eq. (8) that P_{fre} can be calculated if the free field displacement u_i^0 and u_b^0 is known. If only u_b^0 is known, u_i^0 can be solved by Eq. (7). Therefore, only u_b^0 is necessary to calculate P_{fre}. By substituting Eqs. (5) and (8) into Eq. (4), P_{eff} can be calculated be the equation below:

$$P_{eff} = M_{bi}^{\Omega^0}\ddot{u}_i^0 + M_{bb}^{\Omega^0}\ddot{u}_b^0 + C_{bi}^{\Omega^0}\dot{u}_i^0 + C_{bb}^{\Omega^0}\dot{u}_b^0 + K_{bi}^{\Omega^0}u_i^0 + K_{bb}^{\Omega^0}u_b^0 + C_b\dot{u}_b^0 + K_b u_b^0 \tag{9}$$

In Eq. (9), the subscript of these submatrices used to calculate the effective forces only involve bb and bi, indicating that only a single-layer element in the domain Ω^0 is required to be adjacent to Γ. This single-layer domain lies between Γ and Γ_i as shown in Fig. 2(b). Therefore, as long as the local model and the free field model share the same layer between Γ and Γ_i, Eq. (9) can be expressed by using the matrices in the domain Ω instead of Ω^0, as shown in Eq. (10), which is very easy to realize in modeling.

$$P_{eff} = M_{bi}^{\Omega}\ddot{u}_i^0 + M_{bb}^{\Omega}\ddot{u}_b^0 + C_{bi}^{\Omega}\dot{u}_i^0 + C_{bb}^{\Omega}\dot{u}_b^0 + K_{bi}^{\Omega}u_i^0 + K_{bb}^{\Omega}u_b^0 + C_b\dot{u}_b^0 + K_b u_b^0 \tag{10}$$

In such circumstances, only a local model for calculating P_{eff} is needed to solve Eq. (3).

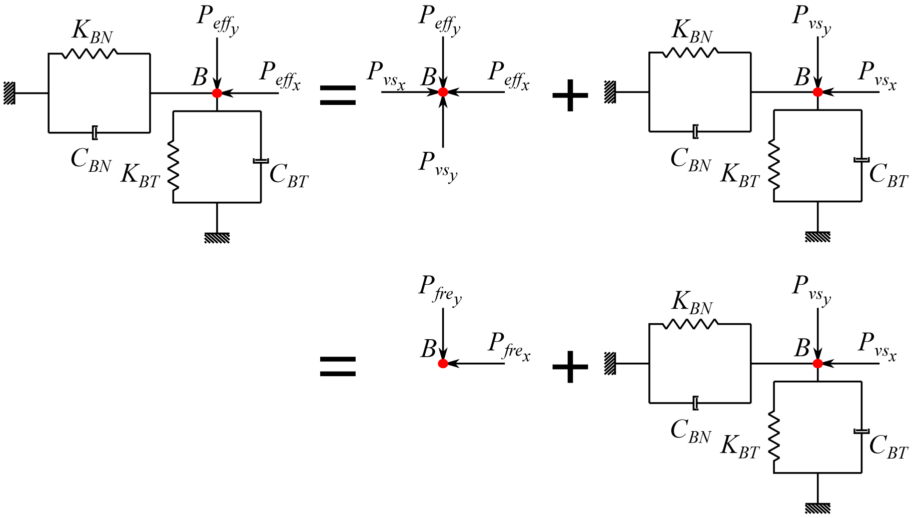

Fig. 3. Decomposition of effective nodal forces in SLDM.

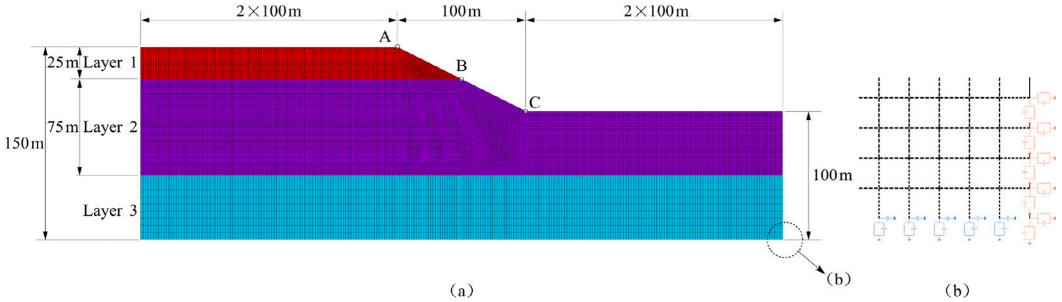

Fig. 4. (a) Finite element model of the slope and dimensions, A, B and C are the three observation points (b) Details of the HBM boundary at corner.

2.3. Implementation

The implementation of HBM should follow this computation procedure: (I) Using the numerical or analytical solution of 1D P/SV wave motion to approximated the free field motion on the crest and toe side lateral boundaries, respectively. (II) Calculate the effective loads P_{eff} on the lateral boundary from the free field motions obtained in step I by Eq. (10). (III) Calculate the effective loads on the bottom boundary by Eq. (1) or Eq. (2). These effective loads on the lateral and bottom boundaries are applied simultaneously to the slope model to realize the seismic excitation.

Note that no superposition was used in the derivation procedure of P_{eff} in SLDM, and the Joyner's method can be used in nonlinear analysis, It is possible to perform nonlinear analysis with the HBM. All that need to change in the formulation are the stiffness terms in Eqs. (3) and (10), which depend on the material constitutive equations.

3. Verification

In this section, finite element models of a slope site will be established to validate the proposed method. Since there is no analytical solution available for slope site responses analysis, the verification procedure can be divided into two steps: the verification of the bottom boundary and the verification of the combination of the bottom and lateral boundaries. The verification of the bottom boundary has been verified by Luo [18]. In Luo's verification, when using the bottom boundary mentioned above, the maximum relative acceleration error for all depths does not exceed 0.51%. Therefore the first step of verification will not be repeated here. The second step can be verified by a horizontally extended model.

3.1. Modeling

A truncated slope site with a horizontal projection length of 100 meters is shown in Fig. 4. The slope site has three layers, and the linear properties of each layer are shown in Table 1. In finite element modeling, Kuhlemeyer and Lysmer [38] mentioned that 1% error requires at least 12 nodes per wavelength. The author believes that the number of nodes required for each wavelength should be an integer power of 2 in order to accurately simulate the peaks and valley of the smallest wavelength. Therefore, 16 nodes are required for each wavelength in this paper, and the mesh size can be calculated by the following equation

$$\Delta h = \frac{\lambda_{\min}}{16} = \frac{v_s}{f_{\max}}\frac{1}{16} \tag{11}$$

When using artificial boundaries in the finite element method, Luo et al. [39] mentioned that the distance between the observation point and the artificial boundary should be no less than twice the width of the local topography. Given all the above requirements, the finite element model using the proposed hybrid boundary method is shown in Fig. 4. To verify the proposed method, an extended meshed model is established. As mentioned earlier, if the width of a finite element model is greater than 7 times its depth, the lateral boundary effects can be neglected [40–42]. In this section, the width of the horizontally extended meshed model for verification is 20 times its depth to avoid an unnecessary scattered wave field, which is much larger than that in previous literature. The horizontally extended model shares the same bottom boundary condition with the HBM model and applies zero vertical(horizontal) displacement condition to the lateral boundary when the model is excited in horizontal(vertical) direction.

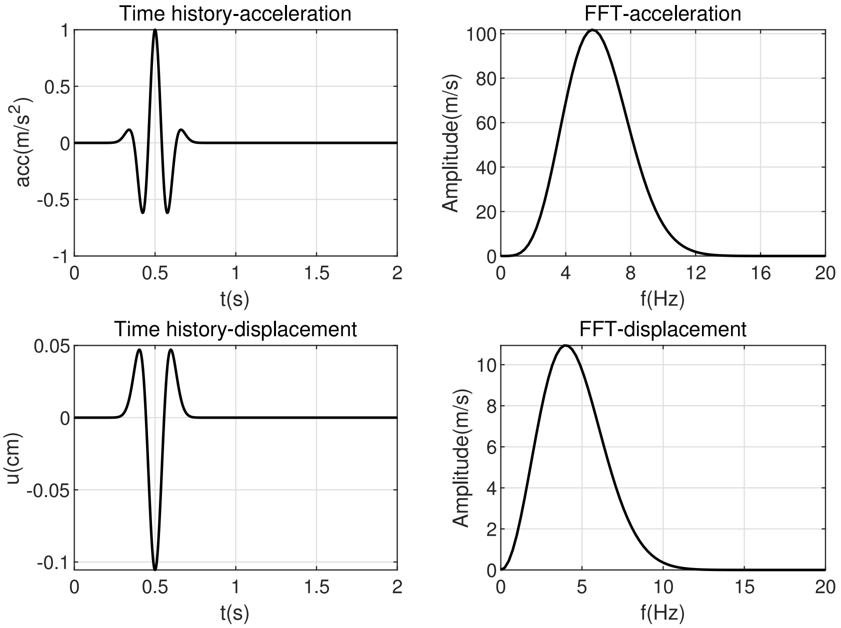

Fig. 5. Time history and FFT of Ricker wavelet.

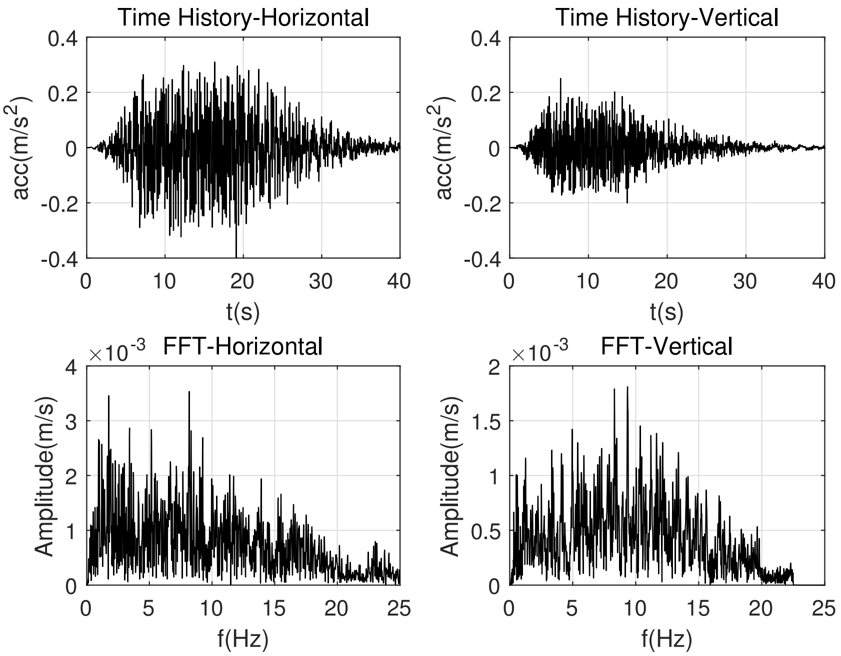

Fig. 6. Time history and FFT of bedrock wave.

Table 1
Linear properties of slope site.

Layer	thickness (m)	Shear wave velocity (m/s)	Density (kg/m^3)	Poisson ratio	Damping ratio
1	25	500	2000	0.3	0.05
2	75	800	2400	0.3	0.05
3	inf	1000	2800	0.3	0.02

A Ricker wavelet [43] and an artificial bedrock motion of Shanghai are selected as input motions. The prevailing frequency of the Ricker displacement is 4 Hz. The time history and FFT plot of the acceleration and displacement of the Ricker wave in the horizontal direction are shown in the Fig. 5. When the Ricker wave is input bidirectionally, the vertical component is 0.65 times the horizontal component. The time history and FFT plots of the horizontal and vertical components of artificial bedrock motion are shown in Fig. 6.

In order to avoid unnecessary errors from using different damping models, all analyses will be performed in the frequency domain by using the hysteresis damping model. Eq. (8) needs to be rewritten as:

$$P_{fre}=M_{bi}^{\Omega 0}\ddot{u}_i^0+M_{bb}^{\Omega 0}\ddot{u}_b^0+(1+2i\xi)\left(K_{bi}^{\Omega 0}u_i^0+K_{bb}^{\Omega 0}u_b^0\right) \tag{12}$$

where ξ is the damping ratio. P_{vs} remains unchanged and P_{eff} can be written as:

$$P_{eff}=M_{bi}^{\Omega}\ddot{u}_i^0+M_{bb}^{\Omega}\ddot{u}_b^0+(1+2i\xi)\left(K_{bi}^{\Omega}u_i^0+K_{bb}^{\Omega}u_b^0\right)+C_b\dot{u}_b+K_bu_b \tag{13}$$

In order to obtain the equations in the frequency domain, the Fourier transform is taken on Eq. (13) with respect to variable time. Eq. (1) is

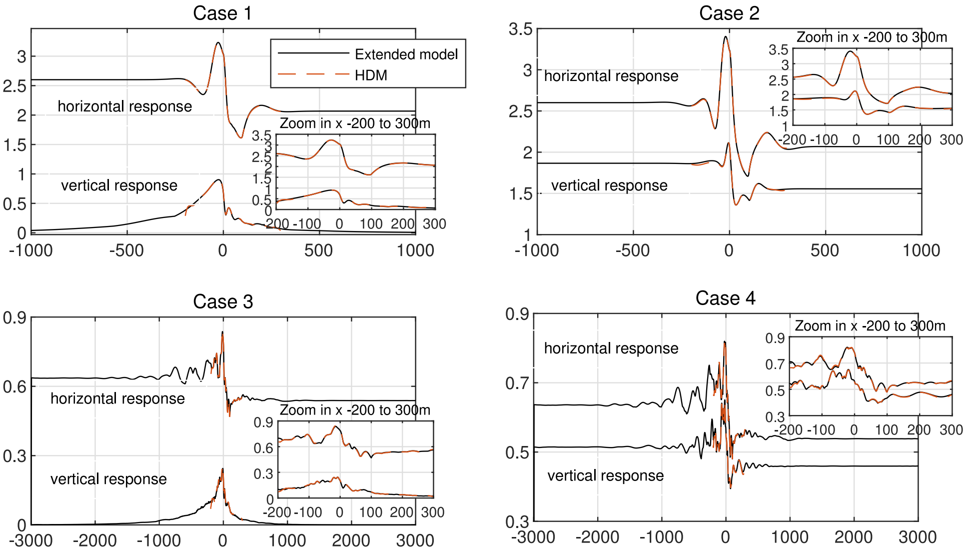

Fig. 7. Comparison of PGA value along the slope surface.

Table 2
Verification analysis cases (x and y denote horizontal and vertical direction).

Cases	Input motion	Excitation direction
1	Ricker wave	Unidirectional x
2	Ricker wave	Bidirectional x+y
3	Bedrock wave	Unidirectional x
4	Bedrock wave	Bidirectional x+y

Table 3
Real elapsed time require for performing different computing model.

Model	Number of degrees-of-freedom	Time required to perform one analysis (s)	
		Unidirection excitation	Bidirectional excitation
Extended model	131 828	790.89	1581.8
HBM	28 620	160.03	163.22

Table 4
PGA results at each observation point.

Analysis cases	Model	A	B	C	A	B	C
		Horizontal response			Vertical response		
1	HBM model (m/s^2)	3.029	1.797	1.654	0.688	0.263	0.192
	Extended model (m/s^2)	3.038	1.800	1.655	0.679	0.262	0.191
	HBM model error (%)	0.292	0.114	0.059	−1.354	−0.142	−0.746
2	HBM model (m/s^2)	3.229	1.940	1.738	2.072	1.414	1.423
	Extended model (m/s^2)	3.235	1.934	1.735	2.073	1.414	1.424
	HBM model error (%)	0.193	−0.306	−0.150	0.050	0.015	0.098
3	HBM model (m/s^2)	0.790	0.573	0.468	0.206	0.090	0.072
	Extended model (m/s^2)	0.788	0.579	0.469	0.202	0.091	0.070
	HBM model error (%)	−0.220	1.120	0.278	−1.920	0.979	−2.010
4	HBM model (m/s^2)	0.778	0.578	0.480	0.556	0.422	0.437
	Extended model (m/s^2)	0.779	0.581	0.480	0.561	0.420	0.434
	HBM model error (%)	0.180	0.492	0.079	0.899	−0.491	−0.664

transformed into frequency domain as follows:

$$\hat{f}(\omega) = 2i\omega\rho v_s \hat{y}(\omega) \tag{14}$$

Eq. (13) is transformed as:

$$\hat{P}_{eff} = \left[-\omega^2 M_{bb}^{\Omega} + (1+2i\xi) K_{bb}^{\Omega} + i\omega C_b + K_b\right] \hat{u}_b^0 + \left[-\omega^2 M_{bi}^{\Omega} + (1+2i\xi) K_{bi}^{\Omega}\right] \hat{u}_i^0 \tag{15}$$

where the caret (ˆ) denotes the Fourier transform of the subtended variable. Then the effective nodal forces in the frequency domain can be calculated and Eq. (6) can be solved in the frequency domain.

The effectiveness of the HBM under unidirectional(horizontal) and bidirectional(horizontal + vertical) excitations are verified and the analysis cases are shown in Table 2. Since the extended model cannot be excited in multiple directions, the results for case 2 and case 4 are the superposition of the results of horizontal excitation only and vertical excitation only.

3.2. Results and discussion

Table 4 shows the PGA results and the relative errors at each observation point shown in Fig. 4 for different analysis cases. The relative errors are computed by Eq. (16):

$$\delta = \frac{v_E - v_o}{v_E} \times 100\% \tag{16}$$

where δ, v_E and v_o denote the percent relative error, the exact value and observed value respectively. Figs. 8 to 11 plot the horizontal and vertical acceleration responses at each observation point for Case 1 to Case 4, respectively. For case 3 and case 4, since the responses have many high-frequency components, plotting all the time histories in a single figure makes the graph unclear. Thus, the results of the extended model and the absolute errors of the HBM model are presented in Figs. 10 and 11. Table 3 shows the degrees of freedom (DOF) of the different models and the time required for an analysis.

Compared with the extended model, HBM significantly improves the computational efficiency. For unidirection and bidirectional excitation cases, it saves about 80% and 90% of the time respectively.

The effectiveness of the HBM are verified under different input motions and excitation directions. When the Ricker wave is excited in the horizontal direction, the maximum errors of the horizontal and vertical acceleration responses are 0.292% and 1.354%, respectively. When the Ricker wave is excited bidirectional, the maximum errors of the horizontal and vertical acceleration responses are 0.306% and 0.098%, respectively. When the bedrock wave is excited in the horizontal direction, the maximum errors of the horizontal and vertical acceleration responses are 1.120% and 2.010%, respectively. And when the bedrock wave is excited bidirectional, the maximum errors of the

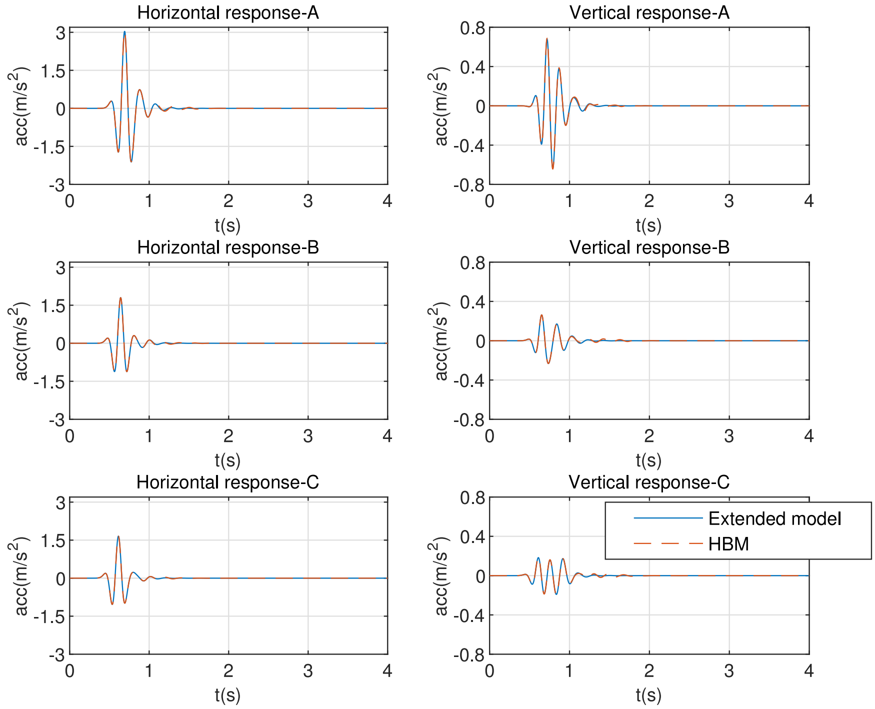

Fig. 8. Comparison of acceleration results at observation points, excites the Ricker wave in the x direction.

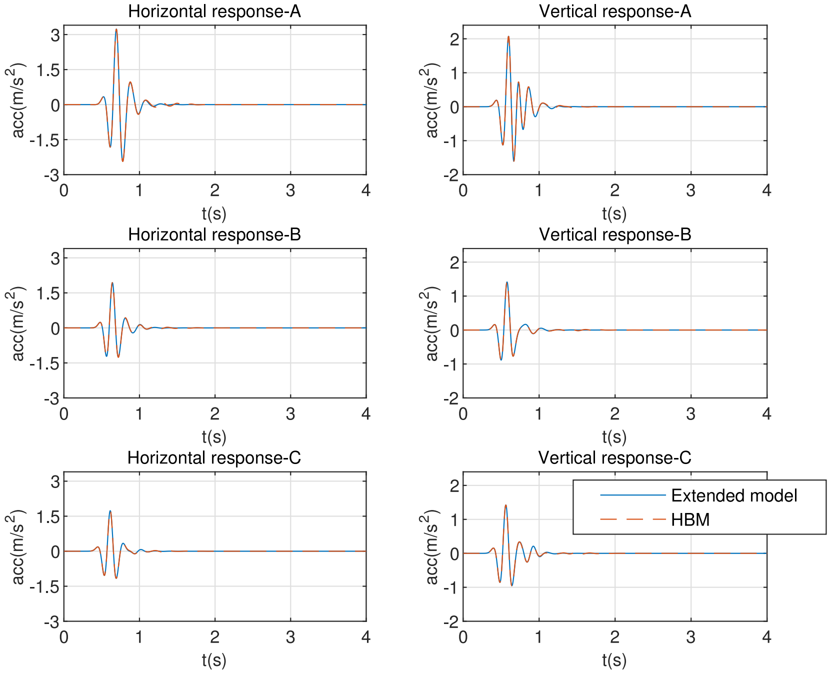

Fig. 9. Comparison of acceleration results at observation points, excites the Ricker wave in the x and y bi-direction.

horizontal and vertical acceleration responses are 0.492% and 0.899%, respectively. Case 3 produces the maximum error among all cases.

In general, for horizontal and vertical acceleration responses, the error of the PGA results when the input motion is the Ricker wave is smaller than the error when the input motion is the bedrock wave. The system becomes silent after 1.5 s when excited by the Ricker wave, as shown in Figs. 8 and 9. Although the HBM still has residual waves in the system after 1.5 s, they do not influence the peaks and valleys of the wave. For bedrock wave with a large number of zero-crossing times, these residual waves can be accumulated and can increase computational errors. Therefore, the results obtained by the HBM when the number of zero-crossing times of the input motion is large have a higher error than when the number is small. For the vertical responses, when the seismic waves are excited bidirectional, the calculation error is smaller than the case where the horizontal motion is excited, while there is no such phenomenon for horizontal responses. A similar phenomenon was also mentioned by Kontoe et al. [44] and Luo et al. [39]. In addition, the free field displacement term in Eq. (2) introduces error, but the results show that this error has little influence on the response.

Table 5
Computation methods.

No.	Methods	Abbr	Freefield motion used in computation
I	HBM	HBM	Mixed free-field motion
II	SLDM	SLMM	Mixed free-field motion
III	SLDM	SLML	Crest side free-field motion
IV	SLDM	SLMR	Toe side free-field motion
V	Rigid base	RBMM	Mixed free-field motion

To further investigate the computational accuracy of the HBM, the PGA value along the slope surface are plotted in Fig. 7. The results show that the HBM and the extend model have good agreements on the PGA value among all the cases. It is also can be observed that the response of the HBM on the crest/toe sides is not always the same as the corresponding free field response. The reason for this phenomenon is the truncated model's scale, which ranges from −200 m to 300 m in this paper, is not big enough to see the stable part of those responses at each side. Especially in case 3 and case 4, the slope topography has a significant influence on the PGA value ranging from −2000 m to 1500 m. This range is greater than the scale of the most truncated FEM model in practice.

It can be concluded that by using only about 10%–20% of the time required to the extended model, the HBM has good performance under different input motions and different excitation directions. Therefore the HBM can be well applied to slope site response or ESSI analysis.

3.3. Influence of slope inclination and damping ratio on the validity of HBM

In this section, two parameters, the slope inclination i and damping ratio ξ are introduced to investigate the validity of HBM under different conditions. Four values of i, 0°, 30°, 60° and 90° and four values of ξ, 0%, 1%, 2% and 5% were chosen for parametric analysis. Figs. 12 and 13 show the PGA response of the extended model and HBM model under different slope inclination i and damping ratio ξ respectively. From Fig. 12, it can be observed that the slope angle i has little influence on the computational accuracy of the HBM. The results of the HBM and the extend model have good agreements among all the analysis cases. Form Fig. 13, the PGA response of the two methods matches well for all the four analysis cases. Meanwhile, At the same time, the higher the damping ratio, the better the performance of the HBM. Thus, it can be concluded that the two parameters, slope angle and damping ratio, has little influence on the computational accuracy when using the HBM. The HBM can be a power tool in site response analysis of slopes.

4. Comparing with conventional methods

The LDM [17] is a powerful tool for simulating semi-infinite bases and has been widely used. In shaking table tests or centrifuge tests, the semi-infinite bases can hardly be simulated. Some plain alluvial sites have soft soil and relatively stiff bedrock. In such circumstances, the fixed based method based on the assumption of rigid bedrock is widely used to simplify modeling and calculations. Both of the LDM and the fixed based method require free-field motion as input motion. However, the free-field motion of slope sites cannot be predicted and can only be approximated by one-dimensional wave propagation analysis on either side of the slope or using their combination. Based on this, the performance of the HBM will be compared with four conventional approaches. The computation methods are shown in Table 5 where the "mixed free-field motion" means that the selection of free-field motion complies with the principle of proximity. In Fig. 14, the left part of the model marked with blue lines uses the crest side free-field motion and the right part marked with red lines uses the toe side free-field motion.

Table 6
PGA results of each method at each observation points (m/s^2).

Analysis cases	Methods	A	B	C	A	B	C
		Horizontal response			Vertical response		
1	Extended model	3.038	1.800	1.655	0.679	0.262	0.191
	HBM	3.029	1.797	1.654	0.688	0.263	0.192
	SLMM	3.054	1.802	1.647	0.700	0.238	0.325
	SLML	3.039	1.801	1.659	0.673	0.273	0.260
	SLMR	3.012	1.797	1.656	0.645	0.261	0.185
	RBMM	2.957	1.774	1.657	1.143	0.673	0.354
2	Extended model	3.235	1.934	1.735	2.073	1.414	1.424
	HBM	3.229	1.940	1.738	2.072	1.414	1.423
	SLMM	3.245	1.925	1.727	2.069	1.407	1.422
	SLML	3.212	1.921	1.733	2.069	1.411	1.421
	SLMR	3.199	1.918	1.725	2.072	1.413	1.424
	RBMM	3.094	1.961	1.814	2.018	1.313	1.307
3	Extended model	0.788	0.579	0.469	0.202	0.091	0.070
	HBM	0.790	0.573	0.468	0.206	0.090	0.072
	SLMM	0.818	0.580	0.474	0.237	0.156	0.118
	SLML	0.794	0.623	0.536	0.249	0.110	0.133
	SLMR	0.982	0.684	0.573	0.349	0.143	0.072
	RBMM	0.900	0.612	0.519	0.676	0.495	0.451
4	Extended model	0.779	0.581	0.480	0.561	0.420	0.434
	HBM	0.778	0.578	0.480	0.556	0.422	0.437
	SLMM	0.812	0.580	0.479	0.538	0.445	0.441
	SLML	0.834	0.626	0.539	0.584	0.390	0.434
	SLMR	0.954	0.681	0.573	0.580	0.394	0.418
	RBMM	0.900	0.612	0.519	0.676	0.495	0.451

Table 7
PGA errors of each method at observation points (%). Bold numbers are values greater than 5%.

Analysis cases	Methods	A	B	C	A	B	C
		Horizontal response			Vertical response		
1	HBM	−0.29	−0.11	−0.06	1.35	0.14	0.75
	SLMM	0.54	0.16	−0.50	3.11	**−9.27**	**70.26**
	SLML	0.05	0.09	0.22	−0.79	3.85	**36.11**
	SLMR	−0.84	−0.16	0.01	**−5.01**	−0.55	−3.37
	RBMM	−2.65	−1.44	0.12	**68.39**	**156.56**	**85.39**
2	HBM	−0.19	0.31	0.15	−0.05	−0.02	−0.10
	SLMM	0.31	−0.45	−0.47	−0.18	−0.49	−0.19
	SLML	−0.73	−0.68	−0.15	−0.19	−0.22	−0.20
	SLMR	−1.11	−0.81	−0.61	−0.01	−0.06	0.00
	RBMM	−4.35	1.39	4.51	−2.64	**−7.11**	**−8.25**
3	HBM	0.22	−1.12	−0.28	1.92	−0.98	2.01
	SLMM	3.78	0.16	0.88	**17.29**	**72.10**	**67.92**
	SLML	0.71	**7.56**	**14.18**	**23.13**	**21.16**	**88.53**
	SLMR	**24.60**	**18.11**	**22.02**	**72.47**	**57.46**	2.50
	RBMM	**14.12**	**5.68**	**10.55**	**234.34**	**444.85**	**541.46**
4	HBM	−0.18	−0.49	−0.08	−0.90	0.49	0.66
	SLMM	4.20	−0.26	−0.21	−4.11	**6.01**	1.56
	SLML	**6.96**	**7.72**	**12.31**	4.19	**−7.15**	0.08
	SLMR	**22.40**	**17.17**	**19.36**	3.42	**−6.02**	−3.74
	RBMM	**15.43**	**5.34**	**8.05**	**20.61**	**18.05**	3.96

Tables 6 and 7 show the PGA values and their errors in different cases, respectively. In order to evaluate the accuracy of each method throughout the entire time history, cosine similarity is introduced as an evaluation indicator. Given two vectors of attributes, A and B, the Cosine similarity between them can be calculated as follows,

$$\text{Similarity} = \frac{\mathbf{A} \times \mathbf{B}}{\|\mathbf{A}\|\,\|\mathbf{B}\|} = \frac{\sum_{i=1}^{n} A_i B_i}{\sqrt{\sum_{i=1}^{n} A_i^2}\sqrt{\sum_{i=1}^{n} B_i^2}} \tag{17}$$

Figs. 15 to 18 show the acceleration results at the observation point A in various cases and the results of the four conventional approaches are compared with the HBM. Again, since the responses of case 3 and case 4 have many high-frequency components, plotting all the time histories in a single figure makes the graph unclear. Thus, in Figs. 17 and 18, the results of the extended model and the absolute errors of the other methods are presented.

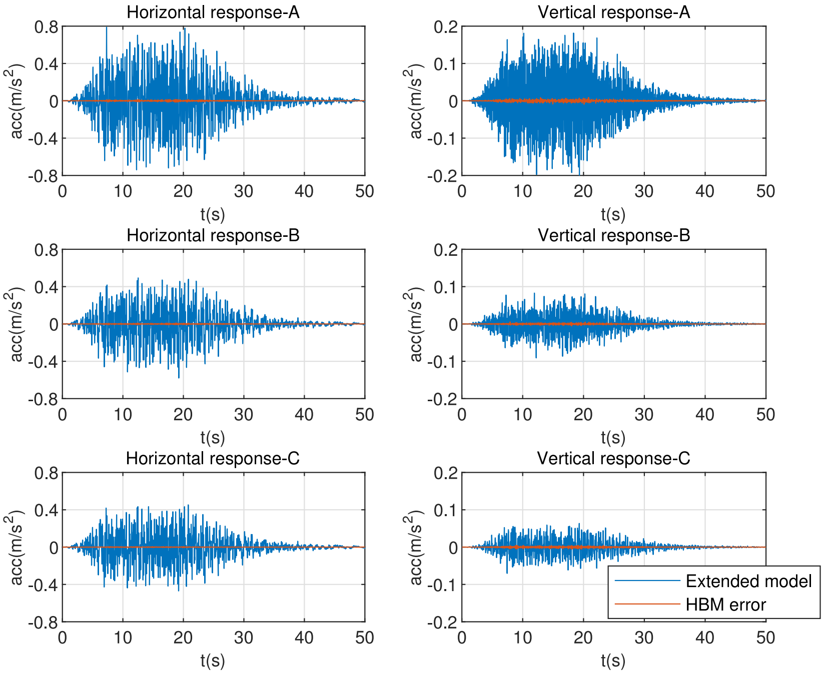

Fig. 10. Comparison of acceleration results at observation points, excites the bedrock wave in the x direction.

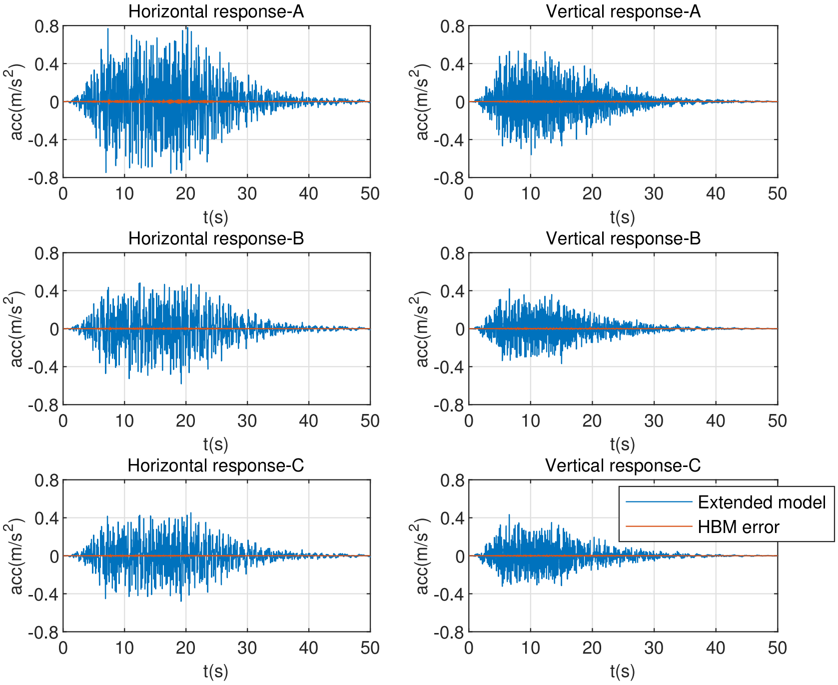

Fig. 11. Comparison of acceleration results at observation points, excites the bedrock wave in the x and y bi-direction.

4.1. General discussion

When the Ricker wave is excited in the horizontal direction, all five approaches listed in Table 5 have good results in horizontal acceleration response, and the maximum error is only 2.65% under the case RBMM. For vertical acceleration response, case 1 shows the best results with an error of 1.35%. However, the results of the other four conventional approaches are not satisfactory, and the maximum error of each method exceeds 5%. When using RBMM, the error at the observation point B even exceeds 100%, which is unacceptable in practice. When the Ricker wave is excited bidirectionally, the error of all methods is relatively small, and the maximum error is 8.25 When the bedrock wave is excited in the horizontal direction, the HBM has good results in both horizontal and vertical responses with a maximum error of only 2.01%, while the four conventional methods have larger errors. The maximum errors of SLMM, SLML, SLMR and RBMM are 72.10%, 88.53%, 72.47% and 541.46%, respectively. When the bedrock wave is excited bidirectionally, the HBM and SLMM both have good results, and the maximum errors of each method are 0.90% and 6.01%, respectively. For SLML, SLMR and RBMM, their respective maximum errors exceed 10%, which are 12.31%, 22.40% and 20.61%, respectively.

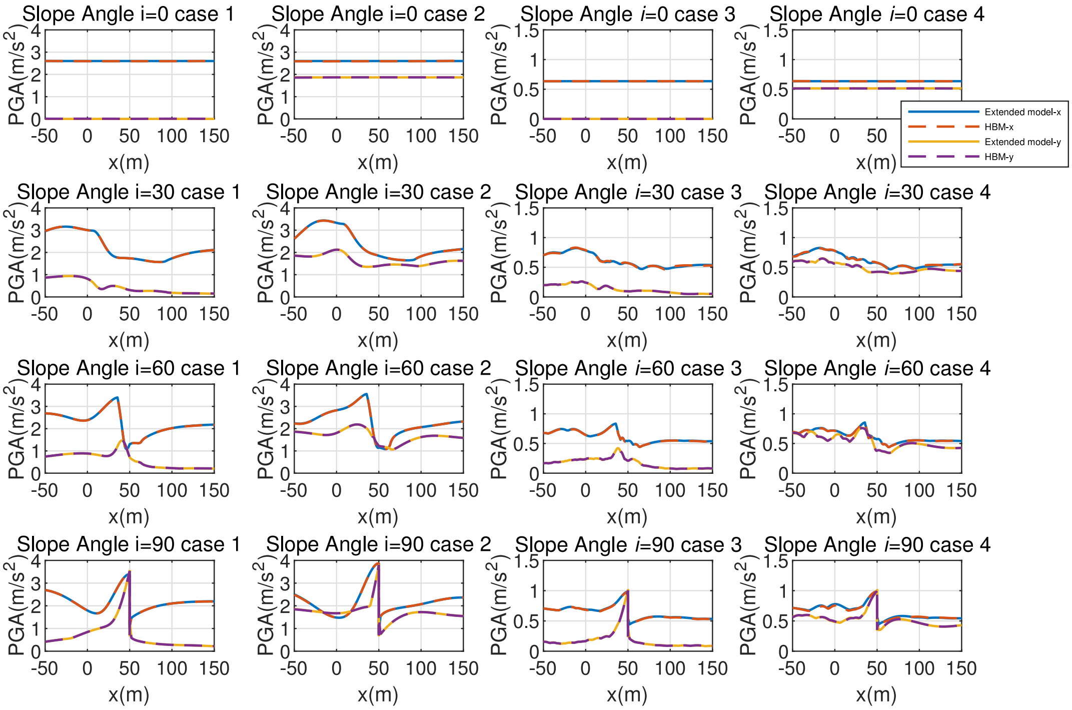

Fig. 12. PGA results under different slope angle *i*.

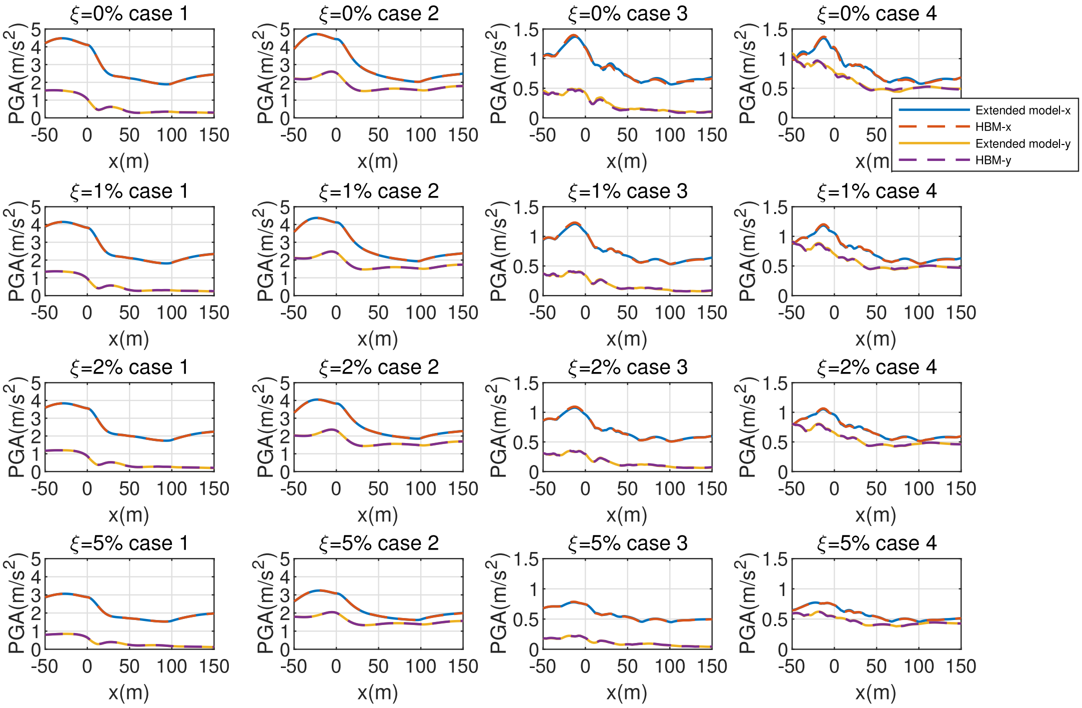

Fig. 13. PGA results under different damping ratio ξ.

In summary, only the HBM has good results in all conditions. The maximum error of the HBM is 2.01%. For the other four conventional methods, the maximum errors are 72.10%, 88.53%, 72.47% and 541.46%, respectively, which are unacceptable in practice. The worst cosine similarities of the five methods in Table 8 are 0.996, 0.623, 0.709, 0.677 and 0.085, respectively. When cosine similarity is used as the evaluation index, the proposed method is also much better than the other four conventional methods.

4.2. Discussion of evaluation indicators, cos similarity vs. PGA

Although the PGA value is a critical parameter in seismic design, the accuracy of each method throughout the time history is also very important in numerical simulation. By comparing Tables 7 and 8, it is obvious that the two parameters, PGA and cosine similarity, are consistent in evaluating the accuracy of numerical simulations in most cases. However, it is worth noting that they are inconsistent in some

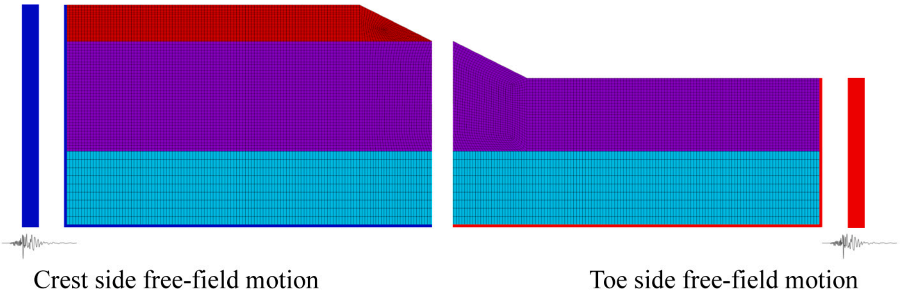

Fig. 14. Mixed free-field motion partition. (For interpretation of the references to color in this figure legend, the reader is referred to the web version of this article.)

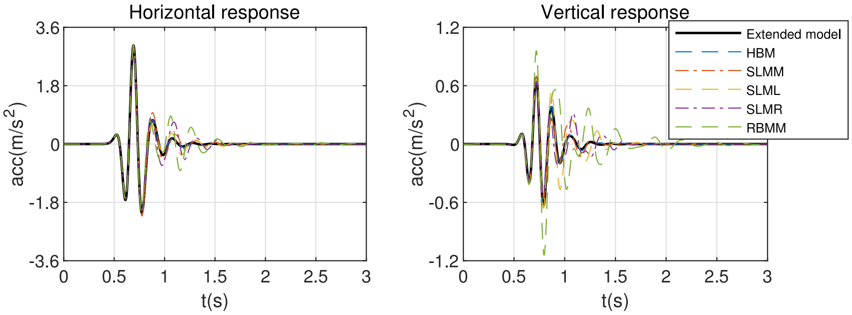

Fig. 15. Comparison of acceleration response at observation points A of different methods, excites the Ricker wave in the x direction.

Table 8
Cosine similarity of time history between the extended meshed model and each method at observation points. Bold numbers are values less than 0.950.

Analysis cases	Methods	A	B	C	A	B	C
		Horizontal response			Vertical response		
1	HBM	1.000	1.000	1.000	0.999	0.997	0.996
	SLMM	0.994	1.000	0.996	0.964	**0.623**	**0.898**
	SLML	0.994	0.985	0.959	**0.930**	**0.872**	**0.836**
	SLMR	0.971	0.966	0.987	**0.881**	**0.806**	**0.746**
	RBMM	**0.928**	0.971	0.969	**0.755**	**0.518**	**0.190**
2	HBM	0.999	1.000	1.000	1.000	1.000	1.000
	SLMM	0.994	0.996	0.997	0.993	0.984	0.992
	SLML	0.994	0.988	0.962	0.985	0.984	0.987
	SLMR	0.978	0.973	0.988	0.986	0.986	0.990
	RBMM	0.927	0.964	**0.922**	**0.883**	**0.747**	**0.713**
3	HBM	1.000	1.000	1.000	0.999	0.998	0.998
	SLMM	0.993	0.999	0.996	**0.909**	**0.633**	**0.839**
	SLML	0.968	**0.943**	**0.905**	**0.920**	**0.791**	**0.709**
	SLMR	**0.931**	**0.892**	**0.930**	**0.767**	**0.677**	**0.788**
	RBMM	**0.945**	0.965	**0.933**	**0.348**	**0.246**	**0.085**
4	HBM	1.000	1.000	1.000	1.000	1.000	1.000
	SLMM	0.993	0.998	0.995	0.982	0.950	0.970
	SLML	0.969	**0.943**	**0.906**	0.983	0.980	0.969
	SLMR	**0.933**	**0.892**	**0.930**	**0.941**	0.961	0.990
	RBMM	0.953	0.969	**0.935**	**0.838**	**0.813**	**0.858**

cases. For example, when comparing the vertical response of the HBM and SLML in Case 1 at observation point A, the result of case HBM has a higher PGA error and a better cosine similarity than those of SLML. In other words, SLML has better results if the evaluation index is PGA, and HBM has better results if the evaluation index is cosine similarity. Such phenomena can be further explored from the results shown in Fig. 15. It is obvious that though SLML has a good fit for PGA in vertical response, its time history results show a significantly larger amplitude than the HBM's after 1 s, which could be accumulated at subsequent peaks. This phenomenon has little influence on the Ricker wave because of its low amount of zero-crossing times. Nevertheless, for seismic waves with significantly high frequencies, such as the bedrock wave used in this paper, the accuracy of PGA will be greatly affected. For example, when using the SLML, the error of the vertical response in Case 3 is much larger than that of Case 1. Therefore, as an evaluation index, cos similarity is a good supplement to PGA.

4.3. Excitation unidirectional or bidirectional

Comparing the results of unidirectional and bidirectional excitation, the Ricker wave and the bedrock wave show similar results. For horizontal responses, the PGA errors of both unidirectional and bidirectional excitation cases are small. However, for vertical responses, the PGA errors of unidirectional excitation cases are much larger than those of bidirectional excitation cases. Such phenomena can be observed from Figs. 15 to 18. One of the reasons for this phenomena is that when the input motion is excited in the horizontal direction, the only vertical response is derivated by the local topography, which is the slope in this paper. The amplitude of this derivated vertical response is much smaller than the total response of the bidirectional excitation cases. Therefore, although the PGA error of the unidirectional excitation cases is not small, it has little influence on the total response of the bidirectional excitation cases. Another reason is that the peak time of the derivated vertical response and the total vertical response are different, which can be observed in Figs. 15 and 16 clearly. In Fig. 15, the peak time of the vertical response is about 0.7 s while in Fig. 16 the peak time of the vertical response is about 0.6 s. This difference in peak time weakens the effect of the derivated vertical response error on the overall vertical response.

4.4. Distribution of PGA and their errors

Fig. 19 shows the PGA distribution along the slope ground surface. The origin of the x-coordinates in these figures are the horizontal location of observation point A, and the x-coordinates of observation points A, B, and C are 0 m, 50 m, and 100 m, respectively. As can be seen from Fig. 19, in terms of accuracy, the HBM has the best results in all the approaches. Among the other four conventional approaches, the results of the SLMM are the best, which only has large errors for vertical response in Case 1 and Case 3. The SLML, SMLR, and RBMM have large errors in Case 3 and Case 4.

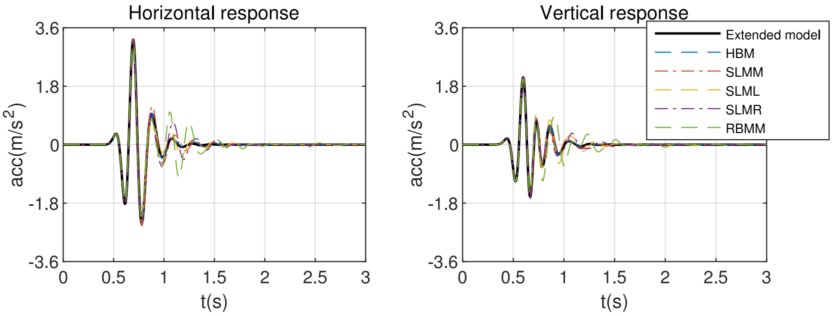

Fig. 16. Comparison of acceleration response at observation points A of different methods, excites the Ricker wave in the x and y bi-direction.

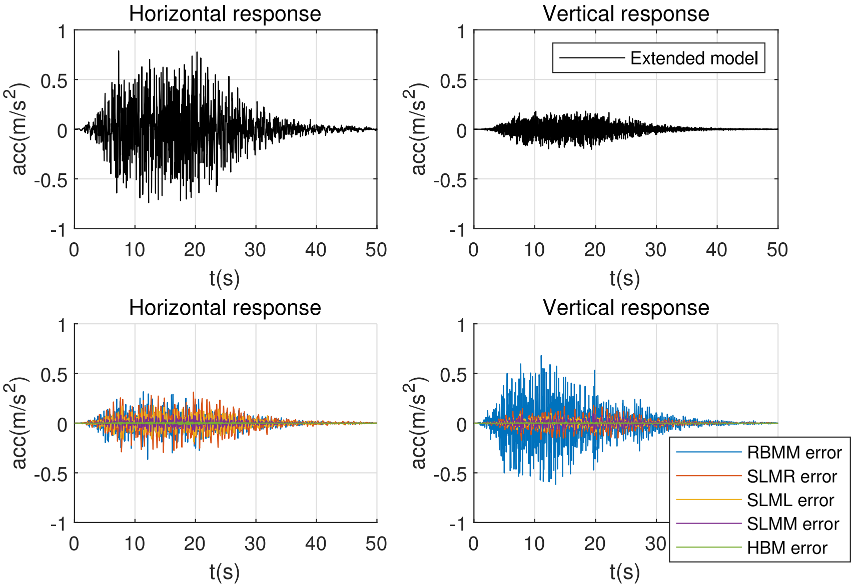

Fig. 17. Comparison of acceleration response at observation points A of different methods, excites the bedrock wave in the x direction.

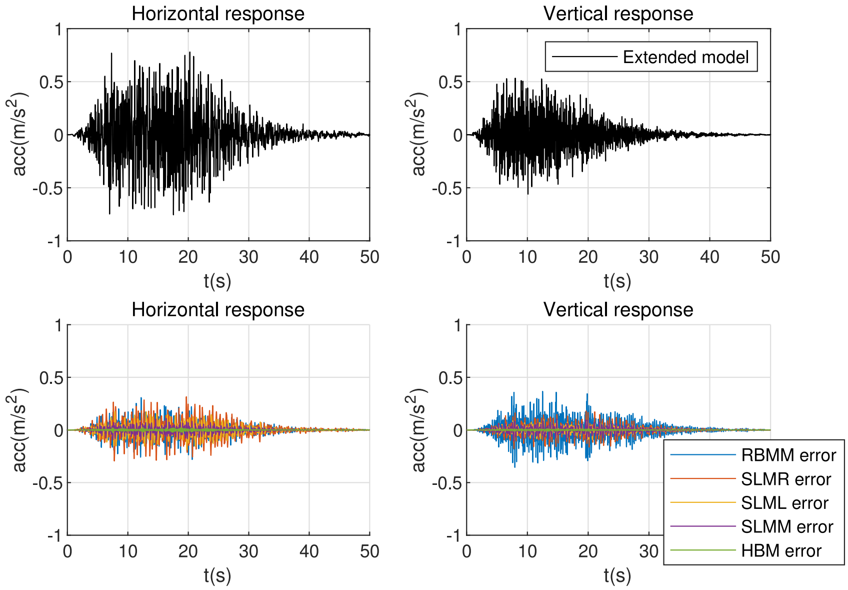

Fig. 18. Comparison of acceleration response at observation points C of different methods, excites the bedrock wave in the x and y bi-direction.

Taking the results between −50 m to 150 m, some useful conclusions can be drawn. Firstly, for all the cases shown in Table 2, their PGA distributions along the slope ground surface are similar. To investigate the distribution of ground motion under different cases, two more cases are introduced for vertical response comparison: case 5: Ricker wave, applied in the vertical direction only and case 6: bedrock wave applied

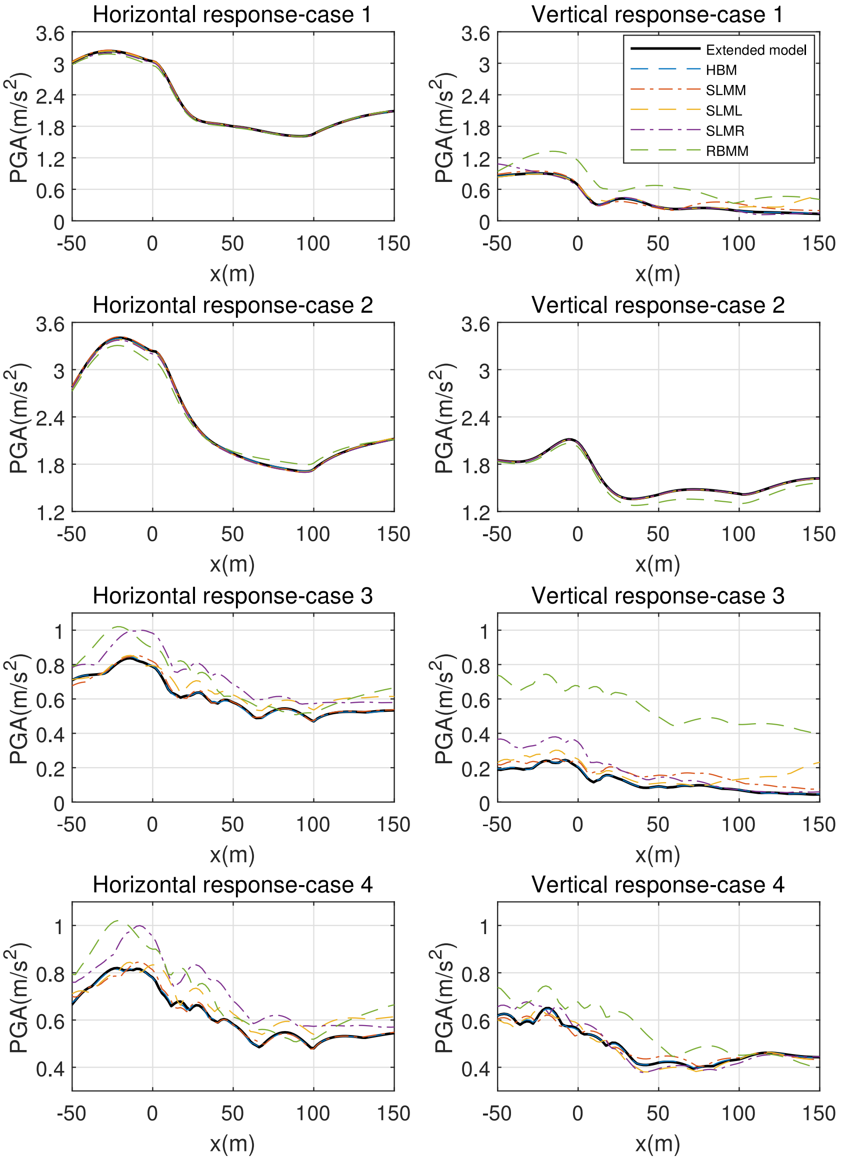

Fig. 19. Comparison of PGA at the slope surface of various cases.

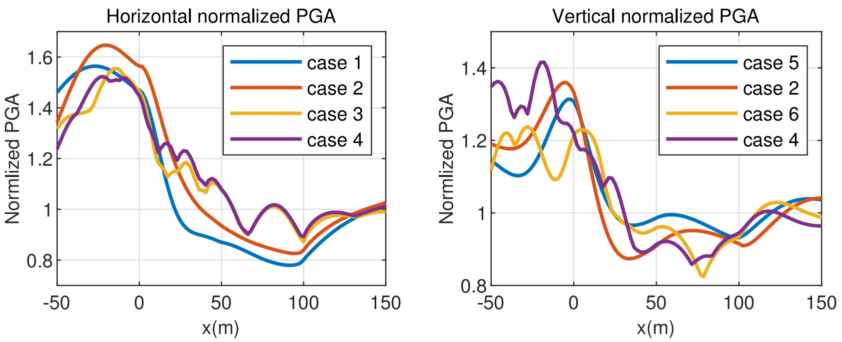

Fig. 20. Normalized PGA on the ground surface of the four cases.

in the vertical direction only. Also, the PGA along the slope surface is normalized. The normalized PGA can be calculated by the following equation:

$$PGA_{normalized} = \frac{PGA_{surface}}{PGA_{toe\,side\,free\,field\,motion}} \tag{18}$$

Fig. 20 shows the normalized PGA for these six cases. Although these four six have different excitation motions and directions, their normalized PGA distributions on the ground surface are similar. In the x-coordinate range of −50 m to 20 m, the horizontally normalized PGA values of all the cases exceed 1, and the values decrease significantly in the range of 0 m to 20 m. The values of the horizontally normalized PGA are about 1 in the x-coordinate range of 20 m to 60 m, are less than 1 in the x-coordinate range of 60 m to 130 m, and approximately back to 1 in the x-coordinate range of 130 m–150 m. The ratio of the maximum to minimum PGA value on the ground surface exceeds 2. The distribution of vertically normalized PGA responses is similar to the distribution of horizontal responses. For all four cases, the vertically normalized PGA results reach a maximum on the crest side and drop down rapidly at the first 20–30 meters on the slope from the crest side to the toe side. In the rest part of the site, the normalized PGA gradually approaches the free-field PGA on the toe side. Similar results also showed by Bouckovalas and Papadimitriou [30], which mentioned a tendency of amplification near the crest and de-amplification near the toe of the slope. When unidirectional ground motion excitation is performed, the maximum derivated vertical response can be as much as 0.45 times of horizontal response on the toe side. When performing bidirectional ground motion excitation, the ratio of the maximum to minimum PGA value on the ground surface exceeds 1.5. In practice, particular attention should be paid to the selection of input motions for structures located near or on the slope and arbitrary selection of input motions may greatly underestimate its PGA value.

5. Conclusion

In this paper, a hybrid boundary method for site response and ESSI analysis of slope sites was proposed. This method handles the bottom and the lateral boundaries separately to achieve semi-infinite excitation. It is suitable for site response analysis of slopes and can also meet the requirements of unidirectional and multidirectional excitation. As long as the distance between the observation point and the lateral artificial boundary is no less than twice the width of the local topography [39], the proposed method can achieve a good balance between modeling scale and accuracy in computation.

A 2D slope model verified the effectiveness of the method under different input motions and excitation directions. Taking an extended model as the exact result, the maximum PGA error of the three observation points in the four analysis cases is only 2.010%. In addition, HBM also has good performance under different slope inclination and damping ratio. The HBM showed high accuracy in the simulation of semi-infinite problems on slope sites.

Four conventional approaches were discussed and compared with the proposed method. The results show that the proposed method has much higher accuracy than the four conventional approaches. The maximum error of all four conventional approaches exceeds 70%. Therefore, improper selection of the excitation method could greatly overestimate the PGA on the slope site.

The consistency of the two parameters, PGA and cos similarity, as indicators for evaluating the accuracy of the time history response were also discussed. These two evaluation indicators were consistent in most cases, but inconsistent in some specific cases. In practice, cos similarity can be a good complement to PGA.

The PGA distribution along the slope surface was discussed. A normalized PGA was introduced to compare the PGA distribution under different input motions and excitation directions. The results show that amplification of ground motion occurred on the crest side, while de-amplification of ground motion occurred on the toe side. The ratio of the maximum and minimum normalized PGA on the ground surface could exceed 2. Therefore, great attention should be paid to the spatial variability of ground motion on slope sites in practice.

CRediT authorship contribution statement

Hao Wang: Investigation, Validation, Writing - original draft, Writing - review & editing, Funding acquisition. **Chao Luo:** Conceptualization, Methodology, Writing - review & editing, Funding acquisition. **Jun-Zhou Wan:** Formal analysis, Visualization. **Meng-Fan Zhu:** Formal analysis, Writing - review & editing. **Meng-Lin Lou:** Conceptualization, Supervision, Funding acquisition. **Huai-Ping Feng:** Resources, Supervision, Funding acquisition.

Declaration of competing interest

The authors declare that they have no known competing financial interests or personal relationships that could have appeared to influence the work reported in this paper.

Acknowledgments

The authors deeply appreciate four anonymous reviewers for the careful review of the manuscript, the thoughtful remarks and criticism that helped improving the paper. This work presented was sponsored by the Natural Science Foundation of Hebei Province, China under Grant numbers E2019210350, E2019210245 and E2019210356, the project for the introduction of overseas students in Hebei Province, China under Grant numbers C20190363 and C20190364, independent project for State Key Laboratory of Mechanical Behavior and System Safety of Traffic Engineering Structures, China under Grant number ZZ2020-04 and ZZ2021-03, and National Natural Science Foundation of China under Grand number 51808359. These supports are gratefully acknowledged.

References

[1] Boussinesq J. Équilibre d' élasticité d' un sol isotrope sans pesanteur, supportant différents poids. C R Math Acad Sci Paris 1878;86(86):1260–3, (in French).

[2] Lamb H. On waves in an elastic plate. Proc R Soc A 1917;93(648):114–28. http://dx.doi.org/10.1098/rspa.1917.0008.

[3] Mindlin RD. Force at a point in the interior of a semi-infinite solid. Physics 1936;7(5):195–202. http://dx.doi.org/10.1063/1.1745385.

[4] Green G. An essay on the application of mathematical analysis to the theories of electricity and magnetism. Nottingham, England: T. Wheelhouse; 1828.

[5] Haskell NA. The dispersion of surface waves on multilayered media. Bull Seismol Soc Am 1953;43(1):17.

[6] Tompson WT. Transmission of elastic waves through a stratified soil medium.. J Appl Phys 1953;43(1):17. http://dx.doi.org/10.1063/1.1699629.

[7] Kausel E, Roësset JM. Stiffness matrices for layered soils. Bull Seismol Soc Am 1981;71(6):1743.

[8] Alterman Z, Karal Jr FC. Propagation of elastic waves in layered media by finite difference methods. Bull Seismol Soc Am 1968;58(1):367.

[9] Lysmer J, Kuhlemeyer RL. Finite dynamic model for infinite media. J Eng Mech Div 1969;95(4):859–78.

[10] White W, Valliappan S, K. Lee I. Unified boundary finite dynamic models. J Eng Mech Div 1977;103(5):949–64.

[11] Akiyoshi T. Compatible viscous boundary for discrete models. J Eng Mech Div 1978;104(5):1253–66.

[12] Deeks AJ, Randolph MF. Axisymmetric time-domain transmitting boundaries. J Eng Mech 1994;120(1):25–42. http://dx.doi.org/10.1061/(ASCE)0733-9399(1994)120:1(25).

[13] Liu J, Li B. A unified viscous-spring artificial boundary for 3-d static and dynamic applications. Sci China E 2005;48(5):570–84. http://dx.doi.org/10.1360/04ye0362.

[14] Du X, Zhao M. A local time-domain transmitting boundary for simulating cylindrical elastic wave propagation in infinite media. Soil Dyn Earthq Eng 2010;30(10):937–46. http://dx.doi.org/10.1016/j.soildyn.2010.04.004.

[15] Joyner WB, Chen ATF. Calculation of nonlinear ground response in earthquakes. Bull Seismol Soc Am 1975;65(5):1315.

[16] Yasui Y, Takano S, Takeda T, Miyamoto A, Kurimoto O, Ishikawa R. Finite element method for obliquely incident seismic wave problems. In Proceedings of the ninth world conference on earthquake engineering. Japan, 1988, p. 447–52. 2.

[17] Liu J, Lu Y. A direct method for analysis of dynamic soil-structure interaction based on interface idea. In: Chuhan Z, Wolf JP, editors. Dynamic soil-structure interaction. Developments in geotechnical engineering, vol. 83, Elsevier; 1998, p. 261–76. http://dx.doi.org/10.1016/S0165-1250(98)80018-7.

[18] Luo C. On effect of river valley topography and soil-structure interaction for seismic response of long-span bridges (Ph.D. thesis), Shanghai, China: Tongji University; 2017, (in Chinese).

[19] Bielak J, Loukakis K, Hisada Y, Yoshimura C. Domain reduction method for three-dimensional earthquake modeling in localized regions, part I: theory. Bull Seismol Soc Am 2003;93(2):817–24. http://dx.doi.org/10.1785/0120010251.

[20] Yoshimura C, Bielak J, Hisada Y, Fernandez A. Domain reduction method for three-dimensional earthquake modeling in localized regions, part II: Verification and applications. Bull Seismol Soc Am 2003;93(2):825–40. http://dx.doi.org/10.1785/0120010252.

[21] Jeremic B, Jie G, Preisig M, Tafazzoli N. Time domain simulation of soil-foundation-structure interaction in non-uniform soils. Earthq Eng Struct Dyn 2009;38(5):699–718. http://dx.doi.org/10.1002/eqe.896.

[22] Kontoe S, Zdravkovic L, Menkiti C, Potts D. Seismic response and interaction of complex soil retaining systems. Comput Geotech 2012;39:17–26. http://dx.doi.org/10.1016/j.compgeo.2011.08.003.

[23] Isbiliroglu Y, Taborda R, Bielak J. Coupled soil-structure interaction effects of building clusters during earthquakes. Earthq Spectra 2015;31(1):463–500. http://dx.doi.org/10.1193/102412EQS315M.

[24] Solberg JM, Hossain Q, Mseis G. Nonlinear time-domain soil–structure interaction analysis of embedded reactor structures subjected to earthquake loads. Nucl Eng Des 2016;304:100–24. http://dx.doi.org/10.1016/j.nucengdes.2016.04.026.

[25] Poursartip B, Fathi A, Kallivokas LF. Seismic wave amplification by topographic features: A parametric study. Soil Dyn Earthq Eng 2017;92:503–27. http://dx.doi.org/10.1016/j.soildyn.2016.10.031.

[26] Abell JA, Orbović N, McCallen DB, Jeremic B. Earthquake soil-structure interaction of nuclear power plants, differences in response to 3-D, 3 × 1-D, and 1-D excitations. Earthq Eng Struct Dyn 2018;47(6):1478–95. http://dx.doi.org/10.1002/eqe.3026.

[27] Poursartip B, Kallivokas LF. Model dimensionality effects on the amplification of seismic waves. Soil Dyn Earthq Eng 2018;113:572–92. http://dx.doi.org/10.1016/j.soildyn.2018.06.012.

[28] Ashford SA, Sitar N, Lysmer J, Deng N. Topographic effects on the seismic response of steep slopes. Bull Seismol Soc Am 1997;87(3):701.

[29] Ashford SA, Sitar N. Analysis of topographic amplification of inclined shear waves in a steep coastal bluff. Bull Seismol Soc Am 1997;87(3):692.

[30] Bouckovalas GD, Papadimitriou AG. Numerical evaluation of slope topography effects on seismic ground motion. Soil Dyn Earthq Eng 2005;25(7–10):547–58. http://dx.doi.org/10.1016/j.soildyn.2004.11.008.

[31] Tripe R, Kontoe S, Wong TKC. Slope topography effects on ground motion in the presence of deep soil layers. Soil Dyn Earthq Eng 2013;50:72–84. http://dx.doi.org/10.1016/j.soildyn.2013.02.011.

[32] Rizzitano S, Cascone E, Biondi G. Coupling of topographic and stratigraphic effects on seismic response of slopes through 2D linear and equivalent linear analyses. Soil Dyn Earthq Eng 2014;67:66–84. http://dx.doi.org/10.1016/j.soildyn.2014.09.003.

[33] Wartman J, Seed RB, Bray JD. Shaking table modeling of seismically induced deformations in slopes. J Geotech Geoenviron Eng 2005;131(5):610–22. http://dx.doi.org/10.1061/(ASCE)1090-0241(2005)131:4(610).

[34] Nova-Roessig L, Sitar N. Centrifuge model studies of the seismic response of reinforced soil slopes. J Geotech Geoenviron Eng 2006;132(3):388–400. http://dx.doi.org/10.1061/(ASCE)1090-0241(2006)132:3(388).

[35] Jafarzadeh F, Shahrabi MM, Farahi Jahromi H. On the role of topographic amplification in seismic slope instabilities. J Rock Mech Geotech Eng 2015;7(2):163–70. http://dx.doi.org/10.1016/j.jrmge.2015.02.009.

[36] Jeong S, Asimaki D, Dafni J, Wartman J. How topography-dependent are topographic effects? Complementary numerical modeling of centrifuge experiments. Soil Dyn Earthq Eng 2019;116:654–67. http://dx.doi.org/10.1016/j.soildyn.2018.10.028.

[37] Chopra A. Dynamics of structures: Theory and applications to earthquake engineering. Civil engineering and engineering mechanics series, Prentice Hall; 2012, URL: https://books.google.com/books?id=3cctkgEACAAJ.

[38] Kuhlemeyer RL, Lysmer J. Finite element method accuracy for wave propagation problems. J Soil Mech Found Div 1973;99(5):421–7.

[39] Luo C, Lou M-L, Gui G-Q, Wang H. A modified domain reduction method for numerical simulation of wave propagation in localized regions. Earthq Eng Eng Vib 2019;18(1):35–52. http://dx.doi.org/10.1007/s11803-019-0488-7.

[40] Lou M-L, Pan D-G, Fan L-C. Effect of vertical artificial boundary on seismic response of soil layer. J Tongji Univ (Nat Sci) 2003;31(7):757–61, (in Chinese).

[41] Chen Q-J, Yang Y-S. Effect of lateral artificial boundary on random seismic response of soil layer. Rock Soil Mech 2011;32(11):3442–7, (in Chinese).

[42] Qiao G-D, Lou M-L. Effect of vertical artificial boundary on seismic responses analysis of large-scale open caisson. Eng Mech 2012;S1:111–4, (in Chinese).

[43] Mavroeidis GP, Papageorgiou AS. A mathematical representation of near-fault ground motions. Bull Seismol Soc Am 2003;93(3):1099–131. http://dx.doi.org/10.1785/0120020100.

[44] Kontoe S, Zdravkovic L, Potts DM. An assessment of the domain reduction method as an advanced boundary condition and some pitfalls in the use of conventional absorbing boundaries. Int J Numer Anal Methods Geomech 2009;33(3):309–30. http://dx.doi.org/10.1002/nag.713.